INVESTIGATION OF CRYSTAL GEOMETRIES FOR FIBER COUPLED GAMMA IMAGING INTRA-OPERATIVE PROBES

Martin P. Tornai, Craig S. Levin, Lawrence R. MacDonald, Edward J. Hoffman

Division of Nuclear Medicine and Biophysics, Department of Molecular and Medical Pharmacology, UCLA School of Medicine, Los Angeles, CA 90095

ABSTRACT

In this work, gamma sensitive intra-operative imaging detectors using CsI(Na), CsI(Tl) and NaI(Tl) scintillators coupled through optical fibers were investigated with simulations and measurements. Three coupling methods were employed between the detectors and optical fiber imaging array: discrete crystals coupled one-to-one with the fibers; discrete crystals coupled through a light diffuser to an unmatched fiber array; and continuous, light sharing crystals coupled directly to the fiber optic array. The discrete crystals were arranged in 4x4 element arrays of sizes ranging from 1x1x2.5 mm^3 up to 2x2x6 mm^3. CsI(Na) had the best pulse height and single crystal energy resolution (44% at 140 keV) when coupled through fibers to the MC-PMT photodetector. All discrete arrays were completely resolved, indicating that the intrinsic spatial resolution corresponded to the crystal size. The spatial resolution for the 12.5 mm ϕ x 3.5 mm continuous crystals was ~1.2 mm FWHM, with relative pulse heights of 1.5 to 5.5 times lower than for the discrete array detectors.

I. INTRODUCTION

Complete resection of malignant cancers has been shown to increase the life span of patients nearly twice as long as partial resection [1], and e.g. in neurosurgery, to increase the quality of life for those patients [2]. The problem in neurosurgery lies in identification of residual tumor, which is currently determined by contrast CT or MRI in addition to the surgeons' impressions. Histological samples are also taken and analyzed during the surgical procedure, but this technique is time consuming and seldom performed [1].

Our investigations of intra-operative imaging probes have led to the development of a new class of fiber-optically coupled imaging devices [3-7]. Thick scintillators offer higher gamma stopping efficiencies without the low energy spectral tailing observed in high Z, compound semiconductor imaging detectors of equivalent stopping thicknesses [8,9]. In addition, the fiber-optic light guides insulate the operative cavity from voltage and current sources while facilitating miniaturization of an imaging device. In this work, we investigate gamma sensitive scintillation detectors of various geometries and their characteristics and performance for the proposed imaging task.

II. DETECTOR OPTIMIZATION

A. Detector Candidates

The most important features of scintillation detectors for single photon clinical radiotracers (35 - 370 keV) include high efficiency for the gamma rays, good photofraction, and high light output. CsI(Na) is a most appropriate candidate with relatively high stopping power (Z_{eff}= 54.1, ρ = 4.51 g/cm^3) and light output (39k ph/MeV), wavelength matched (λ_{max} = 420 nm) to bialkali photomultiplier tubes (PMTs). The relatively slow decay time (τ = 630 nsec) is not limiting at the anticipated low *in situ* count rates.

B. Gamma Interactions and Optical Tracking

With a multiple interaction Monte Carlo code [10], gamma rays from a point source of ^{57}Co (122 keV 88%, 136 keV 12%) were simulated to uniformly irradiate single parallel-piped CsI crystals ranging in size from 1x1x2 mm^3 up to 3x3x12 mm^3 by volume. The calculated gamma detection efficiency of CsI for near 140 keV gammas demonstrated that there is a greater dependence on the length of the scintillator than on the cross-sectional area (Fig. 1). The magnitude of the efficiency was approximately 65% higher than for similarly sized NaI(Tl) crystals, which indicates the dependence of efficiency and stopping power on effective Z and density of detector material.

The ΔX, ΔY and ΔZ positions resulting from the multiple scatter interactions and energy deposition at each location were further utilized in optical tracking simulations using DETECT [11]. The optical photon tracking simulations demonstrate a dependence in both the length and cross-sectional area on light collection (Fig. 2).

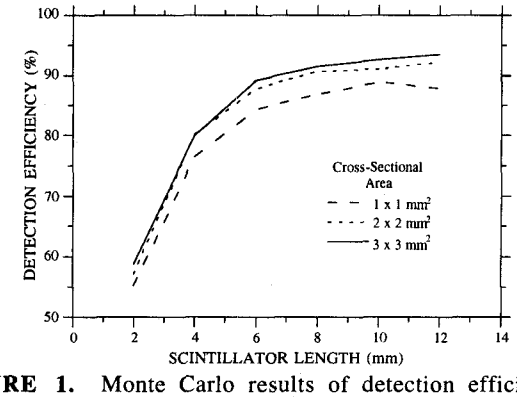

FIGURE 1. Monte Carlo results of detection efficiency of parallel-piped CsI scintillators for ^{57}Co gamma rays.

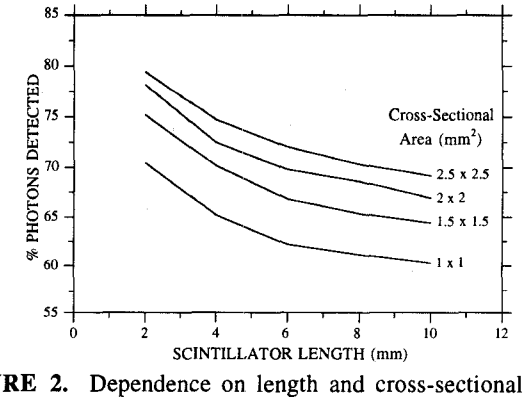

FIGURE 2. Dependence on length and cross-sectional area of photon collection in small parallel-piped scintillators.

0-7803-3534-1/97 10.00©1997IEEE

III. IMAGING DETECTOR ARRAY COMPONENTS

Based on the gamma interaction and optical tracking simulation results, several arrays were acquired and evaluated in different configurations (Fig. 3) for use in the intra-operative gamma imaging probe.

A. Scintillation Detector Arrays

Discrete and continuous CsI crystal detectors were evaluated for use in the fiber-optically coupled gamma imaging probes and compared with a discrete NaI(Tl) array. The 4x4 element discrete detector arrays (Hilger Analytical) utilized TiO_2 as the reflector material. The thickness of the continuous crystals (Advanced Detectors) to ensure modest gamma detection efficiency at ~140 keV (3.5 mm corresponding to ~79% stopping efficiency for large detectors, respectively (cf. Fig. 1)) warranted direct coupling to the optical fibers (Fig. 3, bottom). The addition of a light diffuser between scintillator and optical fibers, as in the beta probe case [6], would have unnecessarily degraded pulse height and energy resolution, as well as spatial resolution.

B. Front-End Fiber Optics

Three methods were evaluated in coupling the detector arrays to the front-end fiber optic bundles of the imaging probe (Fig. 3) including: (1) direct one-to-one crystal-optical fiber coupling; (2) coupling the discrete crystals to the front-end fiber optic array through the use of a light diffuser (discrete, light sharing case); and (3) coupling the continuous crystals directly to the front-end fiber optic array (continuous, light sharing case). Each case was characterized in terms of energy resolution, efficiency, and spatial resolution.

For the one-to-one coupling scheme, the 1x1 mm^2 and 2x2 mm^2 detectors were coupled to 0.925 mm and 2 mm diameter (ϕ), double clad optical fibers (numerical aperture (NA) = 0.72; Kuraray International), respectively, arranged with the same pitch as the 4x4 element scintillator arrays. The 10 cm long optical fibers were embedded in white plastic which acted to support the fibers in the square arrangement, and reflect photons back into the square cross-section crystals that did not make it into the circular cross-section fibers.

The 19 hexagonally arranged, 2 mm ϕ double clad optical fibers previously utilized in the beta imaging probe [4,6] and first implementation of the gamma imaging probe [7] were utilized for the discrete, light sharing case. The front-end of the fiber optic bundle was 12.5 mm in diameter. The 10 cm long hexagonally arranged optical fibers were used to show that one-to-one coupling was not necessary between detector crystals and optical fibers. With this arrangement, any scintillation detector configuration could be utilized on the front-end with a universally adaptable back-end. In essence, an image of the detector array is made, similar in principle to PET block detectors [12], which is then processed to provide spectral and spatial information for each detector element.

In order to make an image of a square detector array with hexagonally arranged fiber optics, a light diffuser was placed between the scintillators and optical fibers. The optimal thickness of the diffuser was determined using the 1x1x4 mm^3 element CsI(Tl) array and hexagonally arranged fibers (Fig. 4). The clear plastic light diffuser thicknesses ranged from 0.48

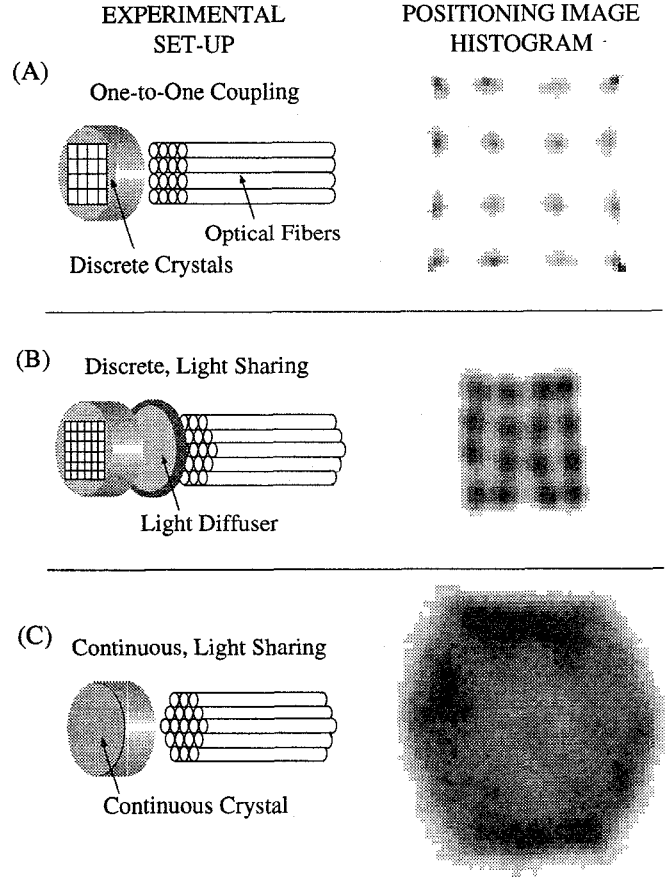

FIGURE 3. Comparison of the experimental coupling between (A) 1x1 mm^2 CsI(Tl) discrete detectors and one-to-one coupled fibers, (B) 1x1 mm^2 CsI(Tl) discrete detectors with light sharing coupling to fibers (NB: one-to-one coupling is not necessary), and (C) 12.5 ϕ x 3.5 mm^2 CsI(Na) continuous crystal detector coupled with intrinsic light sharing to optical fibers.

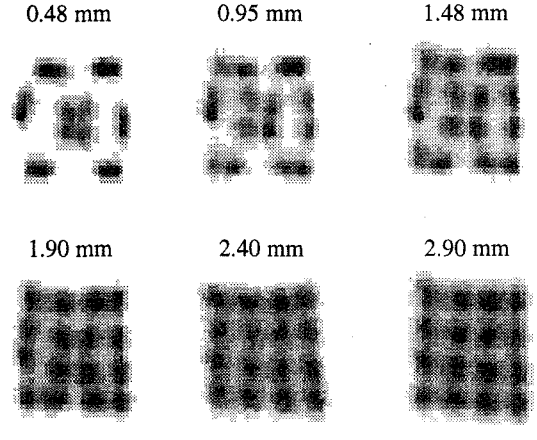

FIGURE 4. Effect of the light diffuser between the 1x1x4 mm^3 element CsI(Tl) crystal array and front-end optical fibers.

mm to 2.9 mm. The best compromise between detector pulse height, resolution of the elements, and sensitivity uniformity (note some detectors are darker than others) was reached with a 1.9 mm thick diffuser.

The continuous crystal light sharing case is intrinsically similar to the continuous crystal beta imaging intra-operative probe [4-6]. Previous simulations and measurements demonstrated that thicker continuous scintillators coupled to fiber

optics have poorer spatial resolution [6,13] due to light spread within the scintillator volume. There are also variations in pulse height response due to depth of interaction effects in these continuous crystals [13]. There were no additional light diffusers used with the continuous crystals as the crystals provided a sufficient area to thickness ratio to expect reasonable spatial resolution.

C. Photodetector and Electronics

The Philips XP1722 multi-channel PMT (MC-PMT) was used as the photon detector. This MC-PMT was previously determined to have optimal characteristics for fiber coupled imaging detectors [6]. The fiber optics (16 square grid or 19 hexagonally arranged fibers) are coupled to discrete detector channels and the parallel outputs feed two distinct resistive charge division networks resulting in four outputs representing signals from the $^{+}$X, $^{-}$X, $^{+}$Y and $^{-}$Y directions. Each output signal has an *i*-V converter/line driver with 2 μsec shaping. The resultant signals are then digitized in list mode with CAMAC ADCs and further processed to form an image with the standard Anger ratio equations.

The charge division network for the hexagonally arranged fibers has independent gain balancing for each channel [6]. This is necessary to ensure uniformity in detection of the light shared signals. The charge division network for the square grid arranged fibers is a different network with no gain balancing of the independent signals. The optical signals from the discrete one-to-one coupled scintillator and fiber optic are not shared, as opposed to the discrete and continuous light sharing cases. The location of the events determined by the Anger ratios are normalized by their pulse amplitude, and so the event positions are completely determined by the values in the charge division circuit [14].

IV. DETECTOR PERFORMANCE

A. Energy Resolution, Pulse Height, and Efficiency

A summary of the results of flood irradiation of the detector arrays with ^{57}Co gammas ($\tau_{1/2}$ = 217d; 122 keV 88%, 136 keV 12%) is presented in Table 1.

Because of the better spectral match of CsI(Na) to the bialkali MC-PMT photocathode, the pulse height of CsI(Na) was greater than of CsI(Tl) (Table 1), and features such as the escape X-rays from CsI were more apparent in the energy spectra (Fig. 5). Several factors account for the relatively small energy resolution improvement of CsI(Na). First, Monte Carlo simulations demonstrated that light collection was dependent on the ratio of area to length of the scintillation crystals (Fig. 2). Next, the TiO_2 reflector, which is optimized for CsI(Tl), is not optimally matched to the emission spectra of CsI(Na). Most important, scintillation photons created distal to the optical fibers (near the gamma ray source) will have a lower pulse height than the same number of photons generated proximal to the optical fiber (deep in the crystal). This depth dependent pulse height variation broadens the photopeak even though the amplitude is greater.

Surprisingly, the light sharing configuration had better pulse heights than the direct, one-to-one configurations (Table 1). The low pulse heights for the NaI(Tl) array are most likely due to the glass plate providing both the hermetic seal and light diffusion for the scintillation photons. For the 1x1 mm^2 cross-section CsI(Tl) crystals, the 67% area coverage of the 0.925 mm ϕ optical fibers caused significant loss in light collection. Note that the more optimally coupled 2x2 mm^2 elements had nearly identical resolution values regardless of the coupling method.

TABLE 1. Summary of various detector array elements' characteristics with ^{57}Co irradiation measured through the optical fibers.

COUPLING / DETECTOR (mm^3)	% FWHM* (at 122 keV)	REL. PULSE HEIGHT*	PIXEL ±σ(%)†
One-to-One Coupling			
NaI(Tl) 2x2x6	61.7 ± 7.3%	59 ± 18%	9.7
CsI(Tl) 1x1x2.5	63.3 ± 7.5%	49 ± 16%	5.8
CsI(Tl) 1x1x4	67.4 ± 8.3%	38 ± 16%	6.8
CsI(Tl) 2x2x4	57.8 ± 6.6%	49 ± 17%	4.0
Discrete, Light Sharing Coupling			
NaI(Tl) 2x2x6	60.4 ± 4.3%	72 ± 21%	4.7
CsI(Tl) 1x1x2.5	57.6 ± 3.0%	56 ± 8%	11.7
CsI(Tl) 1x1x4	57.4 ± 3.9%	47 ± 8%	13.4
CsI(Tl) 2x2x4	55.8 ± 5.3%	53 ± 12%	2.1
CsI(Na) 1.5x1.5x6	51.8 ± 5.1%	100 ± 14%	12.7
Continuous, Light Sharing Coupling			
CsI(Tl) 12.5 ϕ x 3.5	-	18	19.1
CsI(Na) 12.5 ϕ x 3.5	70.6	67	19.0

*Errors are the % standard deviations of the measured values for all the elements in the various detector arrays.
†Defined as the ± standard deviation of the integrated photopeak counts. For the continuous crystals, defined in 75% of the image FOV.

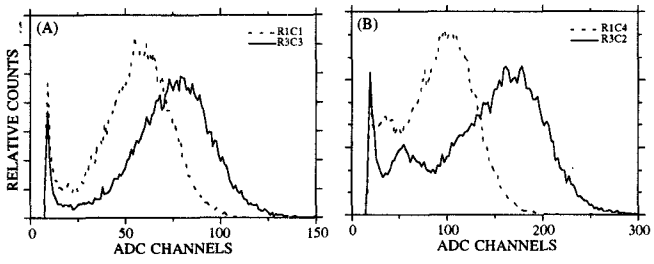

FIGURE 5. Comparison of the measured highest and lowest pulse height responses at 122 keV from the (A) 1x1x4 mm^3 CsI(Tl) and (B) 1.5x1.5x6 mm^3 CsI(Na) arrays. Legends indicate Row and Column elements for various arrays.

The continuous detectors had the poorest overall performance. The scintillation light generated within the detectors is distributed among all fiber elements, thus each optical fiber collects a relatively small fraction of the total light. Additional losses due to the optically absorptive sides, which are necessary for good spatial resolution and linearity, also affect the pulse height and energy resolution of continuous detectors.

An energy window was retrospectively imposed on the list mode data to determine the efficiencies of each crystal. The lower threshold was placed just above the noise shoulder for CsI(Tl) (Fig. 5A), and just above the escape peak for CsI(Na) (Fig. 5B). The integrated counts in these windows represent the relative efficiencies of each crystal. The variation in efficiency was small (right column, Table 1). The efficiency maps for the discrete crystal arrays, after electronic windowing and conversion to the look-up tables, were used as correction maps for spatial resolution and imaging measurements. The continuous crystal measurements used high statistics flood field images as correction maps.

B. *Line Spread Function Responses*

The spatial resolution was measured for some of the light sharing imaging arrays by stepping a 0.3 mm Pb slit collimator and ^{57}Co source in 0.2 mm increments across the faces of the imaging arrays (Fig. 6A and 6B). The slit source was stepped in 1.0 mm increments for the continuous crystals and the LSFs fit with Gaussians (Fig. 6C and 6D).

With a low energy threshold and normalized data, the mean FWHMs were 0.92 ± 0.03 mm, and 1.21 ± 0.07 mm for the 1x1x4 mm^3 CsI(Tl) and 1.5x1.5x6 mm^3 CsI(Na) arrays, respectively. For the discrete crystal arrays, the spatial resolution roughly corresponded to the crystal size.

The resolutions of the continuous crystals varied as a function of light output of the scintillator. The 12.5 ϕ x 3.5 mm^3 continuous CsI(Tl) crystal had a 1.59 ± 0.18 mm and 1.86 ± 0.47 mm FWHM resolution in the X and Y dimensions, respectively. The 12.5 ϕ x 3.5 mm^3 continuous CsI(Na) crystal had a 1.28 ± 0.11 mm and 1.39 ± 0.10 mm FWHM resolution, respectively. The spatial resolution did not, however, improve by the expected 1.9 factor due to the greater pulse height of CsI(Na). These observations, along with others [6] imply that characteristics of the optical fibers, e.g. NA and attenuation length affect the measured resolution as strongly as the light yield of the scintillator.

V. PRELIMINARY IMAGING MEASUREMENTS

Images were made with the 3.5 mm continuous crystals and the 1x1x4 mm^3 CsI(Tl) and 1.5x1.5x6 mm^3 CsI(Na) crystal arrays with light sharing (Fig. 7, top). The transmission phantom consisted of a "stickman" figure, with 1 mm ϕ holes drilled on ~1.2 mm pitch into an 8 mm thick Pb plate. Multiple images were acquired for each detector array and digitally spliced because the phantom was larger than the FOV.

Due to the discrete nature of the two small crystal arrays,

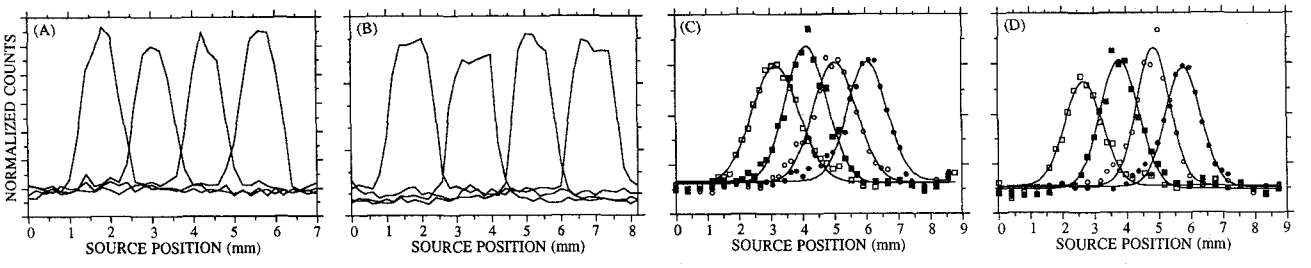

FIGURE 6. Efficiency normalized LSF responses for the (A) 1x1x4 mm^3 CsI(Tl) array, (B) 1.5x1.5x6 mm^3 CsI(Na) array, and the (C) 12.5 ϕ x3.5 mm^3 CsI(Tl) and (D) 12.5 ϕ x3.5 mm^3 CsI(Na) continuous crystals with Gaussian fits to the data.

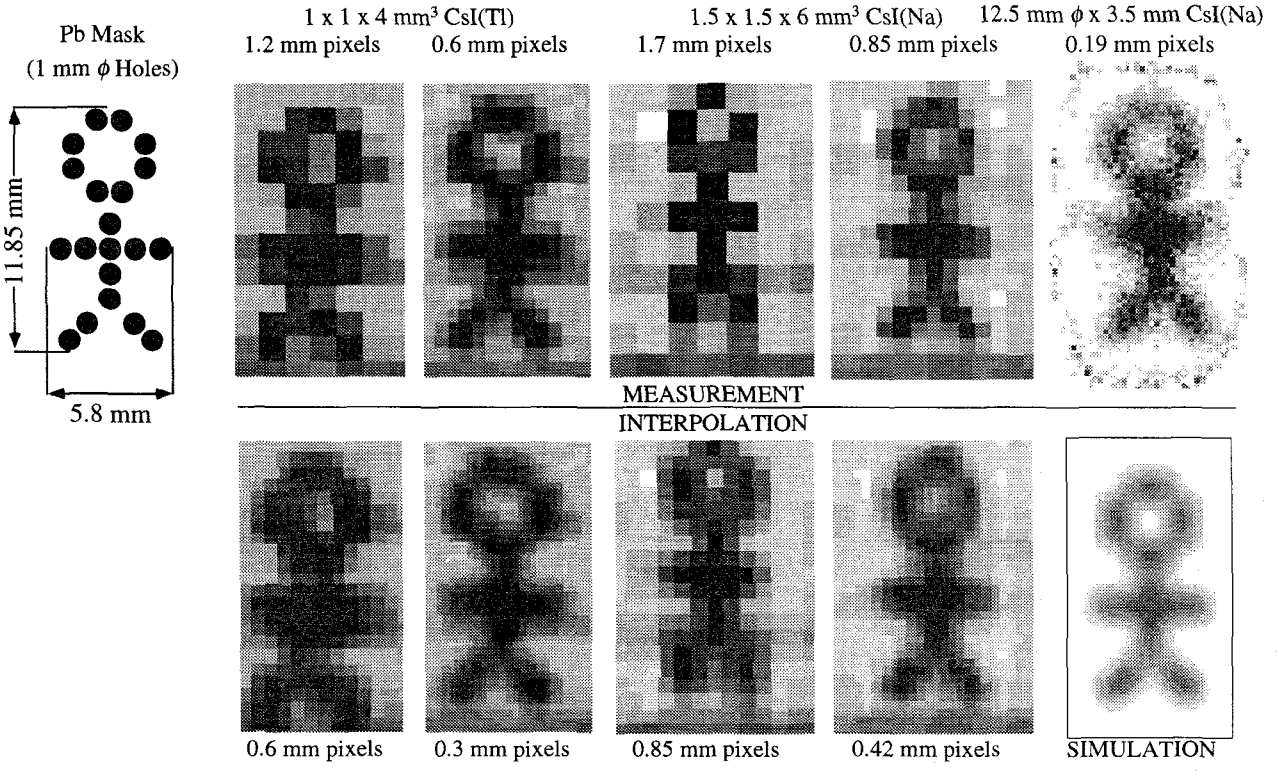

FIGURE 7. Imaging results with various detector arrays of the "stickman" transmission phantom. (Top row) Measured detector results for various sampling schemes and detector arrays. (Bottom row) Digital interpolation of the measured data acts to smooth resultant image. The simulation (lower, far right) was made with the digital transmission phantom on the upper left.

the phantom was subsampled by half-pitch offset measurements to minimize pixellation artifacts in the resultant images. The images collected with the discrete arrays were also digitally smoothed by simple linear interpolation to additionally minimize pixellation in the images (Fig. 7, lower).

The simulated data set (Fig. 7, lower right) was made by 2D Gaussian filtering the digital phantom (Fig. 7, upper left) with the measured intrinsic resolution of the CsI(Na) continuous detector ($\sigma = 0.57$ mm).

VI. CONCLUSIONS

A prototype small area, gamma sensitive detector for intraoperative imaging of residual radiolabeled tumor was successfully developed. The imaging device utilizes parallel-piped and/or continuous scintillation crystals of high stopping power for clinical radioisotopes (e.g. ^{99m}Tc with 140 keV gamma-rays). The best detectors were the CsI(Na) crystals (Table 1), due to the optimal spectral match to the photodetectors, higher light output, and better stopping power compared to other candidates. The detectors were coupled to optical fibers with three schemes: discrete one-to-one coupling of detector, fiber optic and photodetector; discrete crystals coupled through a light diffuser to an unmatched optical fiber bundle; and continuous crystals coupled to the optical fiber array. The fiber optic bundles guide the scintillation light to a MC-PMT with resistive charge division network multiplexing. The output signals are amplified, digitized and digitally processed by the standard Anger positioning difference ratio to form an image positioning histogram. This image histogram can be used as the image itself, as for the continuous crystal implementation, or as the precursor to a look-up table which uniquely identifies each detector and its spectral characteristics.

The discretely coupled one-to-one arrangement allows for complete discretization of the signals along the imaging chain. Each scintillating detector element is uniquely identified by the fiber optic couple to the discrete MC-PMT channel. Crosstalk is minimized both optically, due to the discrete crystals individually coupled to a single fiber, and electronically, due to the small noise contribution from the multiplexing network. Image positioning is determined exclusively by the charge division network.

The continuous light sharing coupled implementation is similar in principle to that developed for the beta imaging intra-operative device [4-6], utilizing most of the same electronics hardware. This implementation has the main advantage that sampling of the activity distributions is continuous. The obtainable spatial resolution is limited by the thickness of the scintillation detector, however. Thinner detectors produce higher spatial resolution images [6,13], while at the same time providing less efficiency for the incident gamma-rays. Depth of interaction effects are also predominant in thick continuous detectors [13], affecting both signal pulse height and spatial resolution.

The discrete, light sharing coupled implementation combines the advantages of both the discrete one-to-one and continuous light sharing coupled systems. The light sharing of the discrete crystals exploits the light channeling from the crystals to the fiber optics through an optimized light diffuser. The light sharing implementation can decode more detectors than MC-PMT channels. This method had both the best mean and individual crystal energy resolutions and pulse heights for any coupling implementation. The same gain balancing hardware that the continuous gamma and beta imaging detectors use was easily utilized. Of the three implementations, this discrete light sharing method was the most versatile and adaptable to existing beta imaging probes.

The development of this class of fiber-optically coupled imaging probes for *in situ* use demonstrates excellent potential. These devices are capable of imaging beta and gamma distributions in tissues. They are compact, yet provide images that can be of clinical value.

ACKNOWLEDGMENTS

The authors thank Hilger Analytical and Advanced Detectors for the crystal arrays and sample crystals, Drs. Jim Telfer, Jan Iwanczyk, Brad Patt, Yiping Shao and Stefan Siegel for useful discussions, and Richard Koziol for expert technical assistance. This work was funded in part by DOE contract DE-FC03-87-ER60615 and NCI grant R01-CA61037.

REFERENCES

[1] PJ Kelly, C Daumas-Duport, DB Kispert, BA Kall, BW Scheithauer, JJ Illig. 1987. Imaging-based stereotaxic serial biopsies in untreated intracranial glial neoplasms. *J. Neurosurg.* **66**(6):865-874.

[2] M Ammirati, N Vick, YL Liao, I Ciric, M Mikhael. 1987. Effect of the extent of surgical resection on survival and quality of life in patients with supratentorial glioblastomas and anaplastic astrocytomas. *Neurosurgery.* **21**(2):201-206.

[3] LR MacDonald, *et al.* 1995. Investigation of the Physical Aspects of Beta Imaging Probes Using Scintillating Fibers and Visible Light Photon Counters. *IEEE Trans. Nucl. Sci.* **NS-42**(4):1351-1357.

[4] MP Tornai, *et al.* 1995. Development of a Small Area Beta Detecting Probe for Intra-Operative Tumor Imaging. *J. Nuc. Med.* **36**(5):109P.

[5] LR MacDonald, *et al.* 1995. Small Area, Fiber Coupled Scintillation Camera for Imaging β-Ray Distributions Intra-Operatively. *Proc. SPIE: Photoelectronic Dets., Cameras and Systems.* **2551**:92-101.

[6] MP Tornai, LR MacDonald, CS Levin, S Siegel, EJ Hoffman. 1996. Design Considerations and Initial Performance of a 1.2 cm^2 Beta Imaging Intra-Operative Probe. *IEEE Trans. Nucl. Sci.* **NS-43**(4):2326-2335, and references therein.

[7] EJ Hoffman, MP Tornai, CS Levin, LR MacDonald, S Siegel. γ and β Intra-Operative Probes. Pres. at *4th Int. Conf. Pos.-Sens. Dets.*, Manchester, EN, 9-13 Sept. 1996 and subm. to *Nucl. Instr. Meth.*

[8] NE Hartsough, *et al.* 1989. Probes Containing Gamma Radiation Detectors for *In Vivo* Tumor Detection and Imaging. *Proc. SPIE: Catheter-Based Sensing and Imaging Technology.* **1068**:92-99.

[9] BE Patt, JS Iwanczyk, MP Tornai, CS Levin, EJ Hoffman. 1995. Development of a Mercuric Iodide Detector Array for Medical Imaging Applications. *Nucl. Instr. Meth.* **A366**:173-182.

[10] Y Shao, SR Cherry, S Siegel, RW Silverman. 1996. A Study of Inter-Crystal Scatter in Small Scintillator Arrays Designed for High Resolution PET Imaging. *IEEE Trans. Nucl. Sci.* **NS-43**(3):1938-1944.

[11] GF Knoll, TF Knoll, TM Henderson. 1988. Light Collection in Scintillating Detector Composites for Neutron Detection. *IEEE Trans. Nucl. Sci.* **NS-35**(1):872-875.

[12] M Dahlbom, EJ Hoffman. 1988. Evaluation of a 2D Array Detector for High Resolution PET. *IEEE Trans. Med. Imag.* **MI-7**:264-272.

[13] S Siegel, SR Cherry, AR Ricci, Y Shao, ME Phelps. 1995. Development of Continuous Detectors for a High Resolution Animal PET System. *IEEE Trans. Nucl. Sci.* **NS-42**(4): 1069-1074.

[14] S Siegel, RW Silverman, Y Shao, SR Cherry. 1996. Simple Charge Division Readouts for Imaging Scintillator Arrays Using a Multi-Channel PMT. *IEEE Trans. Nuc. Sci.* **NS-43**(3):1634-1641.